Violating Bell's inequality with remotely-connected superconducting qubits

Y. P. Zhong,[1] H.-S. Chang,[1] K. J. Satzinger,[1,2] M.-H. Chou,[1,3]
A. Bienfait,[1] C. R. Conner,[1] É. Dumur,[1,4] J. Grebel,[1]
G. A. Peairs,[1,2] R. G. Povey,[1,3] D. I. Schuster,[3] A. N. Cleland[1,4*]

[1]Institute for Molecular Engineering, University of Chicago, Chicago IL 60637, USA
[2]Department of Physics, University of California, Santa Barbara CA 93106, USA
[3]Department of Physics, University of Chicago, Chicago IL 60637, USA
[4]Institute for Molecular Engineering and Materials Science Division,
Argonne National Laboratory, Argonne IL 60439, USA

[*]To whom correspondence should be addressed; E-mail: anc@uchicago.edu.

Quantum communication relies on the efficient generation of entanglement between remote quantum nodes, due to entanglement's key role in achieving and verifying secure communications. Remote entanglement has been realized using a number of different probabilistic schemes, but deterministic remote entanglement has only recently been demonstrated, using a variety of superconducting circuit approaches. However, the deterministic violation of a Bell inequality, a strong measure of quantum correlation, has not to date been demonstrated in a superconducting quantum communication architecture, in part because achieving sufficiently strong correlation requires fast and accurate control of the emission and capture of the entangling photons. Here we present a simple and scalable architecture for achieving this benchmark result in a superconducting system.

Superconducting quantum circuits have made significant progress over the past few years, demonstrating improved qubit lifetimes, higher gate fidelities, and increasing circuit complexity (*1, 2*). Superconducting qubits also offer highly flexible quantum control over other systems, including electromagnetic (*3,4*) and mechanical resonators (*5,6*). These devices are thus appealing for testing quantum communication protocols, with recent demonstrations of deterministic remote state transfer and entanglement generation (*7–9*). The Bell inequality (*10*) is an important benchmark for entanglement, providing a straightforward test of whether a local and deterministic theory can explain measured correlations. To date, however, only local violations of the Bell or Leggett-Garg (*11*) inequalities have been demonstrated using superconducting qubits (*12, 13*), as remote state transfer and entanglement generation with sufficiently high fidelity is still an experimental challenge.

Here we present two distinct methods that violate the Clauser-Horne-Shimony-Holt (CHSH) (*14*) form of the Bell inequality, using a pair of superconducting qubits coupled through a 78 cm-long transmission line, with the photon emission and capture rates controlled by a pair of electrically-tunable couplers (*15*). In one experiment, we use a single standing mode of the transmission line to relay quantum states between the qubits, achieving a transfer fidelity of 0.952 ± 0.009. This enables the deterministic generation of a Bell state with a fidelity of 0.957 ± 0.005. Measurements on this remotely-entangled Bell state achieve a CHSH correlation $S = 2.237 \pm 0.036$, exceeding the classical correlation limit of $|S| \leq 2$ by 6.6 standard deviations. In the second experiment, we control the time-dependent emission and capture rates of itinerant photons through the transmission line, a method independent of transmission distance. These shaped photons enable quantum state transfer with a fidelity of 0.940 ± 0.008, and deterministic generation of a Bell state with a fidelity of 0.936 ± 0.006. Measurements on this Bell state demonstrate a CHSH correlation of $S = 2.223 \pm 0.023$, exceeding the classical limit by 9.7 standard deviations. We note that the Bell state fidelities for both methods

are close to the threshold fidelity of 0.96 for surface code quantum communication (*16*). This simple yet efficient circuit architecture thus provides a powerful tool to explore complex quantum communication protocols and network designs, and can serve as a testbed for distributed implementations of the surface code.

The device layout is shown in Fig. 1**A**, comprising two transmon qubits (*17, 18*), Q_1 and Q_2, connected via two tunable couplers (*15*), G_1 and G_2, to a coplanar waveguide (CPW) transmission line of length $\ell = 0.78$ m. The device is fabricated on a single sapphire substrate, with the serpentine transmission line covering most of the area of a 6×15 mm^2 chip. A circuit diagram is shown in Fig. 1**B**, with more details in the Supplementary Information (SI).

Ignoring the couplers, the transmission line is shorted to ground on both sides, supporting a sequence of standing modes with frequencies equally-spaced by $\omega_{\rm FSR}/2\pi = 1/2T_\ell = 79$ MHz, where $T_\ell = 6.3$ ns is the photon travel time along the line. The coupling strength g_i between qubit Q_i and the nth standing mode is determined by the control signals sent to the coupler G_i, and can be set dynamically between zero and about 45 MHz. The coupling strength is proportional to $\sqrt{n}$, but for the experiments here n is large (~ 70) and the variation of n small ($\sim \pm 5$), so this dependence can be safely ignored. More details can be found in the SI.

When one coupler is set to a small non-zero coupling, with $|g_i| \ll \omega_{\rm FSR}$, and the other coupler is turned off, the coupled qubit can selectively address each standing mode of the transmission line. This is observed by performing qubit spectroscopy, which reveals a sequence of avoided-level crossings with the standing mode resonances (Fig. 1**C**). In the time domain, we observe vacuum Rabi swaps with each mode by first preparing Q_1 in its excited state $|e\rangle$ using a π pulse, then setting the qubit frequency (Fig. 1**D**). The weak coupling allows the qubit to interact with each mode separately, with weak interference fringes visible only near frequencies halfway between each mode.

By weakly coupling both qubits to a single mode, we can relay qubit states through that

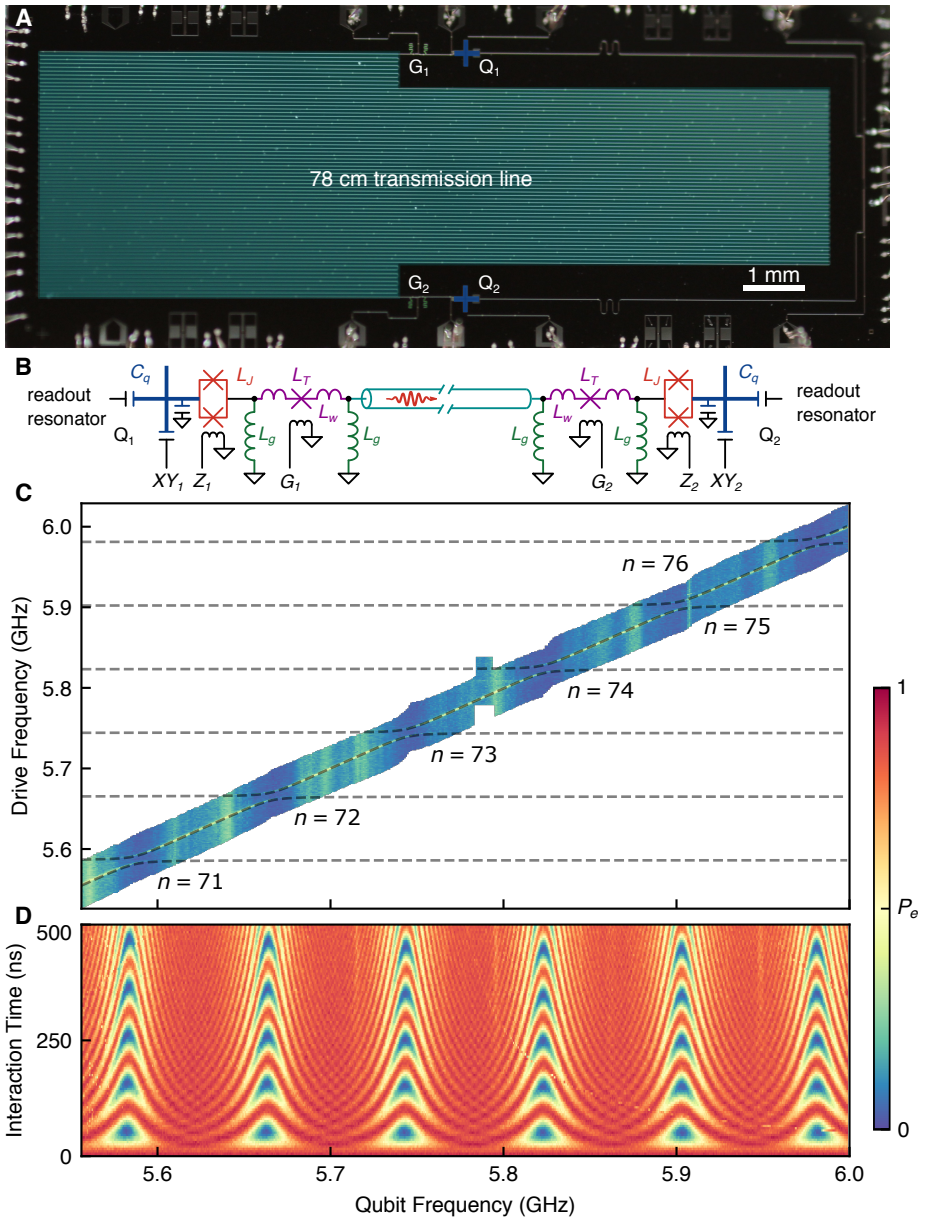

Figure 1: **Device description. A** Photograph of device, showing two qubits Q_1 and Q_2 (blue) connected via tunable couplers G_1 and G_2 (green) to a 78 cm-long coplanar transmission line (cyan). **B** Circuit schematic, with parameters listed in Table S2. **C** Spectroscopy of qubit Q_1 interacting with six transmission line standing modes. Black dashed lines: Numerical simulations. **D** Vacuum Rabi swaps between Q_1 and the six standing modes. The coupling is set to $g_1/2\pi = 5\,\mathrm{MHz} \ll \omega_{\mathrm{FSR}}/2\pi$.

mode (Fig. 2**A**). We prepare Q_1 in its excited state $|e\rangle$, then turn on the G_1 coupling for a time τ, while simultaneously adjusting Q_1's Z bias to match its frequency to the selected mode, swapping the excitation to the mode. We then turn on the G_2 coupling and adjust Q_2's frequency to swap the excitation to Q_2. At $\tau_{\rm swap} = 52$ ns, one photon is completely transferred from Q_1 to Q_2, with a transfer probability of 0.936 ± 0.008. We perform quantum process tomography (*19*) to characterize this transfer process, yielding the process matrix χ_1 shown in Fig. 2**B**, with a process fidelity $\mathcal{F}_1^p = {\rm Tr}(\chi_1 \cdot \chi_{\rm ideal}) = 0.952 \pm 0.009$. Here $\chi_{\rm ideal} = I$ is the ideal process matrix. This experimental result agrees well with the numerically-simulated fidelity $\mathcal{F}_1^p = 0.955$. Note a related experiment (*20*) has demonstrated quantum state transfer through a 1 m-long normal-metal coaxial cable using an innovative "dark" relay mode, achieving a transfer fidelity of 61% with a significantly lossier channel.

We also use the relay mode to generate a Bell state $|\psi_{\rm Bell}\rangle = (|ge\rangle + |eg\rangle)/\sqrt{2}$ between the two qubits, by terminating the Q_1 swap process at the half-swap time $\tau_{\rm half} = 26$ ns. We perform quantum state tomography (*21*), with the reconstructed density matrix ρ_1 displayed in Fig. 2**C**, from which we calculate a state fidelity $\mathcal{F}_1^s = \langle\psi_{\rm Bell}|\rho_1|\psi_{\rm Bell}\rangle = 0.950 \pm 0.005$ and a concurrence $\mathcal{C}_1 = 0.927 \pm 0.013$. Numerical simulations using the master equation give a state fidelity $\mathcal{F}_1^s = 0.947$ and a concurrence $\mathcal{C}_1 = 0.914$, in good agreement with experiment.

We next perform the CHSH Bell inequality test (*12*) on this remotely entangled Bell state (see SI). We measure Q_1 along direction $a = x$ or $a' = y$, and simultaneously measure Q_2 along b or $b' \perp b$, varying the angle θ between a and b (Fig. 2D inset). We then calculate the CHSH correlation S, as shown in Fig. 2**D**. We find that S is maximized at $\theta = 5.5$ rad, where $S = 2.237 \pm 0.036$ with no measurement correction, exceeding the maximum classical value of 2 by 6.6 standard deviations. If we correct for readout error (*12*), we find $S = 2.665 \pm 0.044$, approaching the quantum limit of $2\sqrt{2} \approx 2.828$. The entanglement is deterministic and the measurement is single-shot (see SI), so the detection loophole (*22*) is closed in this experiment.

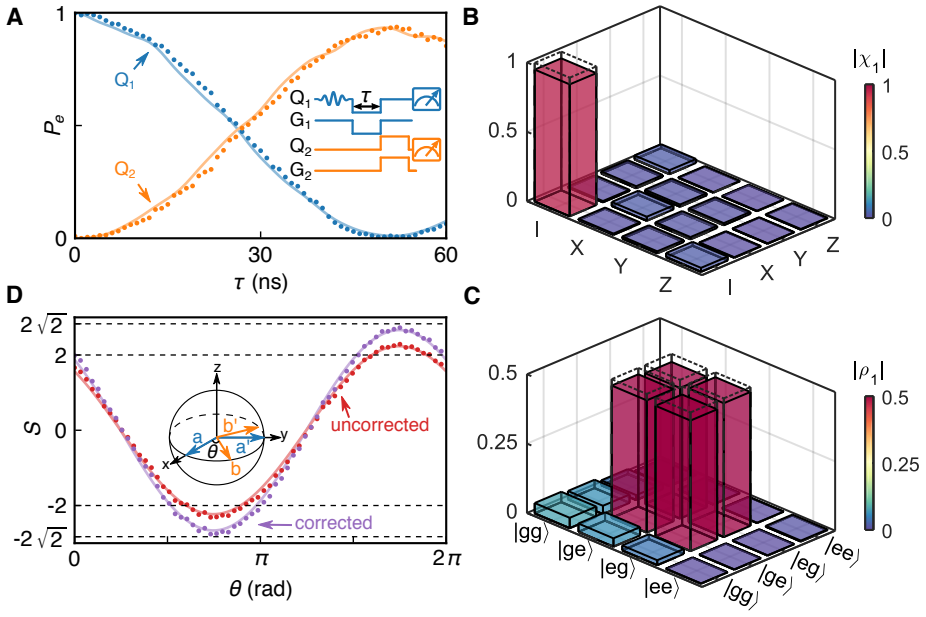

Figure 2: **State transfer, remote entanglement, and Bell violation using the relay method.** **A** Quantum state transfer from Q_1 to Q_2 using the $n = 73$, $\omega_n/2\pi = 5.744$ GHz standing mode as a relay, showing the $|e\rangle$ state probability P_e for each qubit versus swap time τ. Solid lines: Numerical simulations. Inset: Control pulse sequence. **B** Process matrix (absolute values shown as colored bars) of the state transfer process with a fidelity $\mathcal{F}_1^p = 0.952 \pm 0.009$. Dashed-outline frames: Ideal process matrix. **C** Bell state density matrix (absolute values shown as colored bars), with a state fidelity $\mathcal{F}_1^s = 0.950 \pm 0.005$. Dashed-outline frames: Ideal density matrix. **D** Bell test, showing CHSH correlation S versus measurement angle θ. Red dots: No measurement correction; purple dots: With measurement correction. Solid lines: Numerical simulations using ρ_1 from panel **C**. The classical and quantum limits are marked with horizontal dashed lines. Inset: Measurement axes a, a', b, b' on Bloch sphere.

The relay method requires $g_i \ll \omega_{\mathrm{FSR}}$ so that the swap process only involves a single mode. However, ω_{FSR} scales inversely with transmission distance ℓ, making g_i impractically small as ℓ increases. An alternative approach, independent of transmission distance, is to use time-symmetric itinerant photons for state transfer (*23, 24*). This is experimentally challenging, and has only recently been demonstrated with superconducting qubits (*7–9*). In these experiments, quantum states are transferred through a superconducting coaxial cable interrupted by a circulator. The circulator facilitates the state transfer by eliminating retro-reflections in the channel,

but also introduces loss, limiting the transfer fidelity to about 80%. Here we demonstrate remote state transfer and entanglement generation using shaped itinerant photons, with sufficient fidelity to violate the Bell inequality.

In Fig. 3 we show the first part of the itinerant photon method, tuning Q_1's interaction with the transmission line so that Q_1 can play single-photon "ping-pong" with itself. In Fig. 3**A** we show the qubit-transmission line spectroscopy, measured at maximum coupling $|g_1|/2\pi = 45$ MHz, with Q_2's coupling turned off. In this regime, the avoided-level crossing with each mode (Fig. 1**C**) disappears, instead multiple modes are coupled with the qubit. In Fig. 3**B** we perform quantum time-domain reflectometry, where qubit Q_1 is first excited to $|e\rangle$, then we immediately turn the coupling g_1 to its maximum while setting the qubit frequency, both for a duration τ_g, following which we monitor the qubit response. The qubit excitation is released into the transmission line in a few nanoseconds, leaving the qubit in its ground state $|g\rangle$ until the photon reflects off the far end of the transmission line and returns to the qubit, re-exciting the qubit to its $|e\rangle$ state. This process does not depend on qubit frequency, other than some small features. A line cut through the data (Fig. 3**C**) shows that the emission takes about 8 ns, with the round trip then completed in $2T_\ell = 12.6$ ns. Three full transits are shown, with the peak amplitude falling, and small ripples appearing, mainly due to scattering from each photon-qubit interaction. The coupling here is strong enough that the rise and fall time of the control pulse must be accounted for in the simulations (see SI).

To improve the photon capture efficiency, we dynamically tune Q_1's coupling (*23,24*), while keeping the qubit frequency fixed (see SI). The maximum coupling is strong enough that the photon emission and re-capture process can be completed within the round-trip travel time $2T_\ell$, avoiding interference from reflections. However, the bandwidth of our control electronics is insufficient to allow the desired sub-nanosecond tuning of the itinerant photon envelope, so we instead approximately tune the coupler by convolving a Gaussian and a rectangle pulse;

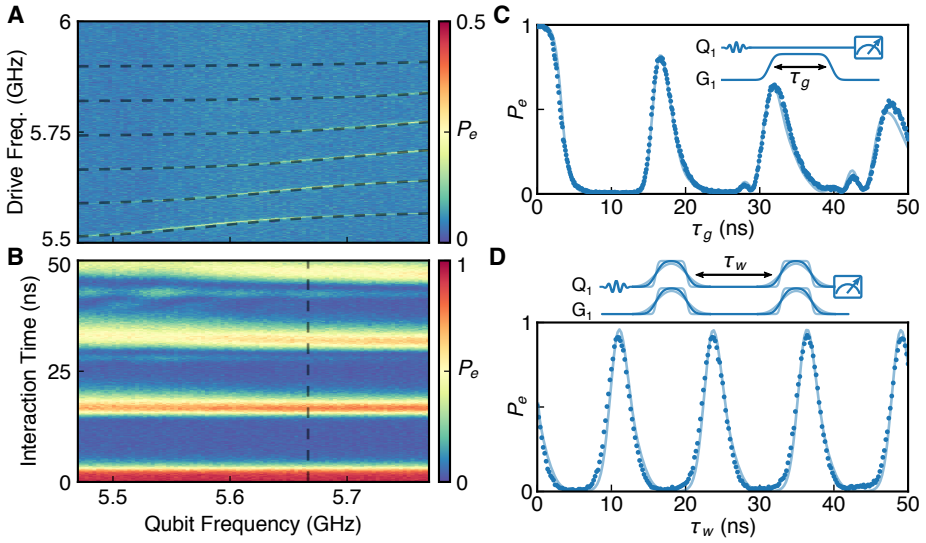

Figure 3: **Single qubit "ping-pong" with itinerant photons.** **A** Qubit Q_1 spectrum when strongly coupled to the transmission line, showing multiple modes interacting with the qubit. Dashed lines: Numerical simulations. **B** Quantum time-domain reflectometry of Q_1 with the transmission line. The coupling is sufficiently strong that the interaction is essentially independent of the qubit frequency. **C** Line cut through data in **B**, showing ping-pong-like dynamics. Q_1 emits an itinerant photon in about 8 ns, which is reflected from the far end of the transmission line and caught by Q_1 a time $2T_\ell = 12.6$ ns later, the process here repeated three times. Solid line: Numerical simulations. Inset: Control pulse sequence, with the rise and fall times indicated. **D** Optimizing photon catch by adjusting control pulse envelope. Maximum catch probability is improved from ~ 0.8 in panel **C** to 0.922 ± 0.004 by adjusting the control pulse slope. Solid line: Numerical simulations. Top: Control pulse sequence, showing the pulse shaping. The qubit bias pulses cancel the coupler-generated frequency shift (see SI).

the width of the Gaussian shapes the edges of the convolved pulse (see SI). We find that this sub-optimal shaping still achieves a self-capture probability of 0.922 ± 0.004 (Fig. 3**D**).

We perform this tune-up for each qubit separately, then combine these processes to perform qubit-to-qubit state transfer using itinerant photons (Fig. 4**A**). We first excite Q_1 to $|e\rangle$, with Q_2 in $|g\rangle$, then turn on the tuned g_1 and g_2 time-dependent couplings simultaneously for a duration t. The itinerant photon is released from Q_1 into the channel in about 10 ns, and begins to interact with Q_2 after $T_\ell = 6.3$ ns. The photon is captured by Q_2, with a maximum probability

of 0.919 ± 0.004 at $t = 12.2$ ns. We carry out quantum process tomography for this sequence, and reconstruct the process matrix χ_2 (see Fig. 4**B**), with a fidelity $\mathcal{F}_2^p = \mathrm{Tr}(\chi_2 \cdot \chi_{\mathrm{ideal}}) = 0.940 \pm 0.008$. Finally, we use half an itinerant photon to generate entanglement between the two qubits: We first prepare Q_1 in $|e\rangle$, then control Q_1's coupling to release half its excitation to the channel, which is captured by Q_2 using the same time-domain coupling as in the state transfer experiment. This generates a Bell state between the two qubits (Fig. 4**C**), with a reconstructed Bell state fidelity $\mathcal{F}_2^s = \langle \psi_{\mathrm{Bell}} | \rho_2 | \psi_{\mathrm{Bell}} \rangle = 0.936 \pm 0.006$ and a concurrence $\mathcal{C}_2 = 0.914 \pm 0.014$.

As with the relay mode method, we carry out a CHSH Bell inequality test with no detection loophole (*22*). We find that S is maximized at $\theta = 0.84$ rad, where $S = 2.223 \pm 0.023$ without applying a measurement correction, exceeding the classical limit of 2 by 9.7 standard deviations. If we correct for readout error, we find $S = 2.629 \pm 0.028$, close to the quantum limit of $2\sqrt{2}$. Note that this method is independent of transmission distance ℓ, so that it should be possible to also close the locality loophole (*25*) by extending the transmission distance.

In conclusion, we present a simple architecture that allows efficient quantum state transfer and remote entanglement between two superconducting qubits, connected by a 78 cm-long transmission line. The fidelities are sufficient to violate the Bell inequality using two different methods. This architecture can be extended to arbitrary distances (limited by the cryostat), expanded to multiple communication channels to explore and test more complex quantum communication protocols, and can serve as a backbone for fault-tolerant distributed quantum computing.

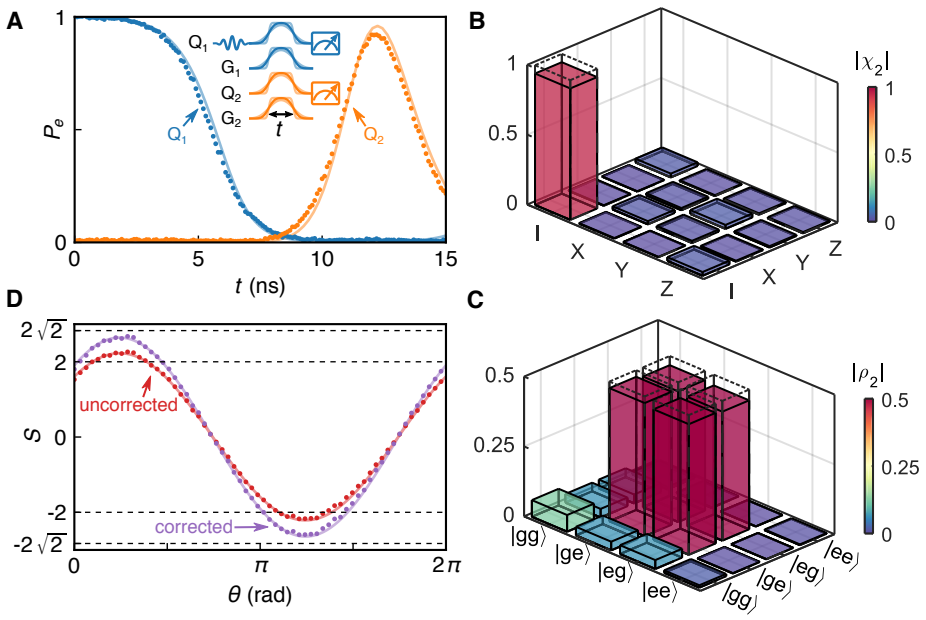

Figure 4: **State transfer, remote entanglement and Bell violation using itinerant photons.** **A** Using optimized control pulses for the couplers while keeping the qubit frequency fixed, we achieve a high-fidelity state transfer, with a maximum transfer probability of 0.919 ± 0.004 in 12.2 ns. Solid lines: Numerical simulations. Inset: Control pulse sequence. **B** Quantum process tomography, with a process fidelity $\mathcal{F}_2^p = 0.940 \pm 0.008$. Dashed-outline frames: Ideal process matrix. **C** Density matrix of the Bell state generated by sending half an itinerant photon from Q_1 to Q_2, with a state fidelity $\mathcal{F}_2^s = 0.936 \pm 0.006$ and a concurrence $\mathcal{C}_2 = 0.914 \pm 0.014$. Dashed-outline frames: Ideal density matrix. **D** Bell test, showing the CHSH correlation S versus measurement angle θ. Red dots: No measurement correction; purple dots: With measurement correction. Solid lines: Numerical simulations using ρ_2 from panel **C**. The correlation is maximized at $\theta = 0.84$ rad, where $S = 2.223 \pm 0.023$ without measurement correction. Classical and quantum limits are marked with horizontal dashed lines.

References

1. M. H. Devoret, R. J. Schoelkopf, *Science* **339**, 1169 (2013).

2. J. Kelly, *et al.*, *Nature* **519**, 66 (2015).

3. M. Hofheinz, *et al.*, *Nature* **459**, 546 (2009).

4. B. Vlastakis, *et al.*, *Science* **342**, 607 (2013).

5. A. D. O'Connell, *et al.*, *Nature* **464**, 697 (2010).

6. Y. Chu, *et al.*, *Science* **358**, 199 (2017).

7. P. Kurpiers, *et al.*, *Nature* **558**, 264 (2018).

8. C. J. Axline, *et al.*, *Nature Physics* **14**, 705 (2018).

9. P. Campagne-Ibarcq, *et al.*, *Physical Review Letters* **120**, 200501 (2018).

10. J. S. Bell, *Physics* **1**, 195 (1964).

11. A. J. Leggett, A. Garg, *Physical Review Letters* **54**, 857 (1985).

12. M. Ansmann, *et al.*, *Nature* **461**, 504 (2009).

13. A. Palacios-Laloy, *et al.*, *Nature Physics* **6**, 442 (2010).

14. J. F. Clauser, M. A. Horne, A. Shimony, R. Holt, *Physical Review Letters* **23**, 880 (1969).

15. Y. Chen, *et al.*, *Physical Review Letters* **113**, 220502 (2014).

16. A. G. Fowler, *et al.*, *Physical Review Letters* **104**, 180503 (2010).

17. J. Koch, *et al.*, *Physical Review A* **76**, 042319 (2007).

18. R. Barends, *et al.*, *Physical Review Letters* **111**, 080502 (2013).

19. M. Neeley, *et al.*, *Nature Physics* **4**, 523 (2008).

20. N. Leung, *et al.*, *arXiv:1804.02028* (2018).

21. M. Steffen, *et al.*, *Physical Review Letters* **97**, 050502 (2006).

22. A. Garg, N. D. Mermin, *Physical Review D* **35**, 3831 (1987).

23. J. I. Cirac, P. Zoller, H. J. Kimble, , H. Mabuchi, *Physical Review Letters* **78**, 3221 (1997).

24. A. N. Korotkov, *Physical Review B* **84**, 014510 (2011).

25. J. Barrett, D. Collins, L. Hardy, A. Kent, *Physical Review A* **66**, 042111 (2002).

26. J. S. Kelly, Fault-tolerant superconducting qubits, Ph.D. thesis, University of California Santa Barbara (2015).

27. A. Dunsworth, *et al.*, *Applied Physics Letters* **112**, 063502 (2018).

28. G. J. Dolan, *Applied Physics Letters* **31**, 337 (1977).

29. A. Dunsworth, *et al.*, *Applied Physics Letters* **111**, 022601 (2017).

30. C. Macklin, *et al.*, *Science* **350**, 307 (2015).

31. D. M. Pozar, *Microwave engineering* (Wiley, 2011), fourth edn.

32. P. Kurpiers, T. Walter, P. Magnard, Y. Salathe, A. Wallraff, *EPJ Quantum Technology* **4**, 8 (2017).

33. D. V. Averin, *et al.*, *Physical Review Letters* **116**, 010501 (2016).

34. M. R. Geller, *et al.*, *Physical Review A* **92**, 012320 (2015).

35. R. Cook, D. I. Schuster, A. N. Cleland, K. Jacobs, *Physical Review A* **98**, 013801 (2018).

Acknowledgments

We thank P. J. Duda for fabrication assistance, and Y. Lu and S. Chakram for helpful discussions. We thank MIT Lincoln Laboratory for providing a traveling-wave parametric amplifier. **Funding:** This effort is supported by the Army Research Office under contract W911NF-15-2-0058. The views and conclusions contained in this document are those of the authors and should not be interpreted as representing the official policies, either expressed or implied, of the Army Research Laboratory or the U.S. Government. The U.S. Government is authorized to reproduce and distribute reprints for Government purposes notwithstanding any copyright notation herein. Devices and experiments were also supported by the Air Force Office of Scientific Research, and by the Department of Energy (DOE). K.J.S. was supported by NSF GRFP (NSF DGE-1144085), É.D. was supported by LDRD funds from Argonne National Laboratory, A.N.C. was supported in part by the DOE, Office of Basic Energy Sciences, and D.I.S. acknowledges support from the David and Lucile Packard Foundation. This work was partially supported by the UChicago MRSEC (NSF DMR-1420709) and made use of the Pritzker Nanofabrication Facility, which receives support from SHyNE, a node of the National Science Foundation's National Nanotechnology Coordinated Infrastructure (NSF NNCI-1542205). **Author contributions:** Y.P.Z. designed and fabricated the devices. Y.P.Z, H.S.C., K.J.S., M.H.C., J.G. and A.N.C. developed the fabrication processes. H.S.C., K.J.S. and A.N.C. contributed to device design. Y.P.Z. performed the experiments and analyzed the data. A.N.C. and D.I.S. advised on all efforts. All authors contributed to discussions and production of the manuscript. **Competing interest:** The authors declare no competing financial interests.

Supplementary materials

Materials and Methods

Supplementary Text

Figs. S1 to S9

Tables S1 to S2

References *(26-35)*

Supplementary Information for

"Violating Bell's inequality with remotely-connected superconducting qubits"

1 Comparison with similar experiments

There have been a number of recent experiments demonstrating deterministic remote state transfer and entanglement generation with superconducting qubits. In Table S1 we tabulate the main results of these experiments and compare with the results reported here.

Source	Transfer efficiency	Process fidelity $\mathcal{F}^p$	State fidelity $\mathcal{F}^s$	Concurrence $\mathcal{C}$	CHSH correlation S
This paper (relay mode)	0.936	0.952	0.950	0.927	2.237
This paper (itinerant photon)	0.919	0.940	0.936	0.914	2.223
Kurpiers *et al.* (*7*)	0.676	0.8002	0.789	0.747	N/A
Axline *et al.* (*8*)	0.74	0.76	0.61	0.51	N/A
Campagne-Ibarcq *et al.* (*9*)	0.7	N/A	0.73	N/A	N/A
Leung *et al.* (*20*)	N/A	0.61	0.793	N/A	N/A

Table S1: Comparison of similar deterministic remote state transfer and entanglement generation experiments on superconducting circuits. Here $\mathcal{F}^p$ is the state transfer process fidelity, $\mathcal{F}^s$ the Bell state fidelity, $\mathcal{C}$ the Bell state concurrence, and S the CHSH correlation.

2 Device fabrication

Most of the fabrication is done on 100 mm-diameter sapphire substrates, with steps 5-7 typically completed on quarters cut from the larger wafer. This recipe is adapted in part from refs. (*26,27*).

1. 100 nm Al base layer deposition using electron beam evaporation.

2. Base layer lithography and dry etch with BCl_3/Cl_2/Ar inductively coupled plasma. This

defines the qubit capacitors, the tunable coupler wiring, the 78 cm-long transmission line, and the readout and control circuitry.

3. 1 μm crossover scaffold SiO_2 deposition using electron beam evaporation and liftoff, using an optically-patterned PMMA/nLOF2020 bilayer. The thin PMMA layer serves as a protection layer for the base Al layer from step 1 during the development of nLOF2020 in AZ300 MIF. The PMMA is then removed with a downstream O_2 plasma ash after development.

4. 500 nm crossover Al deposition with the same liftoff patterning method as step 3. The Al deposition is preceded by an *in situ* Ar-ion mill without breaking vacuum between these two steps.

5. Josephson junction deposition using the Dolan bridge method (*28*) shadow evaporation and liftoff, using a PMMA/MAA bilayer and electron beam lithography. The Al evaporated in this step does not contact the base wiring and is not preceded by an Ar ion mill.

6. Bandage Al liftoff deposition (*29*), preceded by an *in situ* Ar ion mill. This step establishes galvanic connections between the base wiring Al from step 1 and the Josephson junctions defined in step 5.

7. Vapor HF to remove the SiO_2 scaffold underlying the Al crossovers.

We use electron beam evaporation to deposit each film. We use photolithography with 0.9 μm I-line photoresist (AZ MiR 703) for steps 2 and 6. Each liftoff step is in N-methyl-2-pyrrolidone at 80°C.

3 Experimental setup

Figure S1 shows the overall control and readout electronics layout. We use custom digital-to-analog converter (DAC) and analog-to-digital converter (ADC) circuit boards for qubit control and measurement, respectively. The control boards have dual-channel 14-bit vertical resolution DAC integrated circuits operating at 1 Gs/s, and the measurement boards have dual-channel 8-bit vertical resolution ADC integrated circuits operating at 1 Gs/s. Each control signal output and measurement signal input channel is filtered by a custom Gaussian low-pass filter with 250 MHz bandwidth. The control boards are used to generate nanosecond-length pulses for fast qubit Z or coupler G control, or to provide the modulation envelope for several-GHz carrier signals, the two combined using an IQ mixer. In this application the signals are used to implement qubit XY rotations, or to drive the readout resonator feed-line for qubit state measurements. In the latter case, the output signal from the readout feed-line is first amplified by a traveling wave parametric amplifier (*30*) (TWPA) at the mixing chamber stage with close to quantum-limited added noise, then amplified by a cryogenic high electron mobility transistor (Low Noise Factory HEMT) at the 4 K stage, and further amplified by two room-temperature Miteq HEMT amplifiers, before down-conversion with an IQ mixer and capture by the measurement ADC board. Two cryogenic circulators with low insertion loss are added between the TWPA and the cryogenic HEMT to block reflections as well as noise emitted from the input of the cryogenic HEMT. An additional circulator is inserted between the TWPA drive line and the qubit, to avoid any unexpected excitation of the qubits from the TWPA drive signal. The measurement board has an on-board demodulation function which allows for fast demodulation of the captured waveform. Each control line is heavily attenuated and filtered at each temperature stage in the dilution refrigerator to minimize the impact on the qubit coherence while retaining controllability.

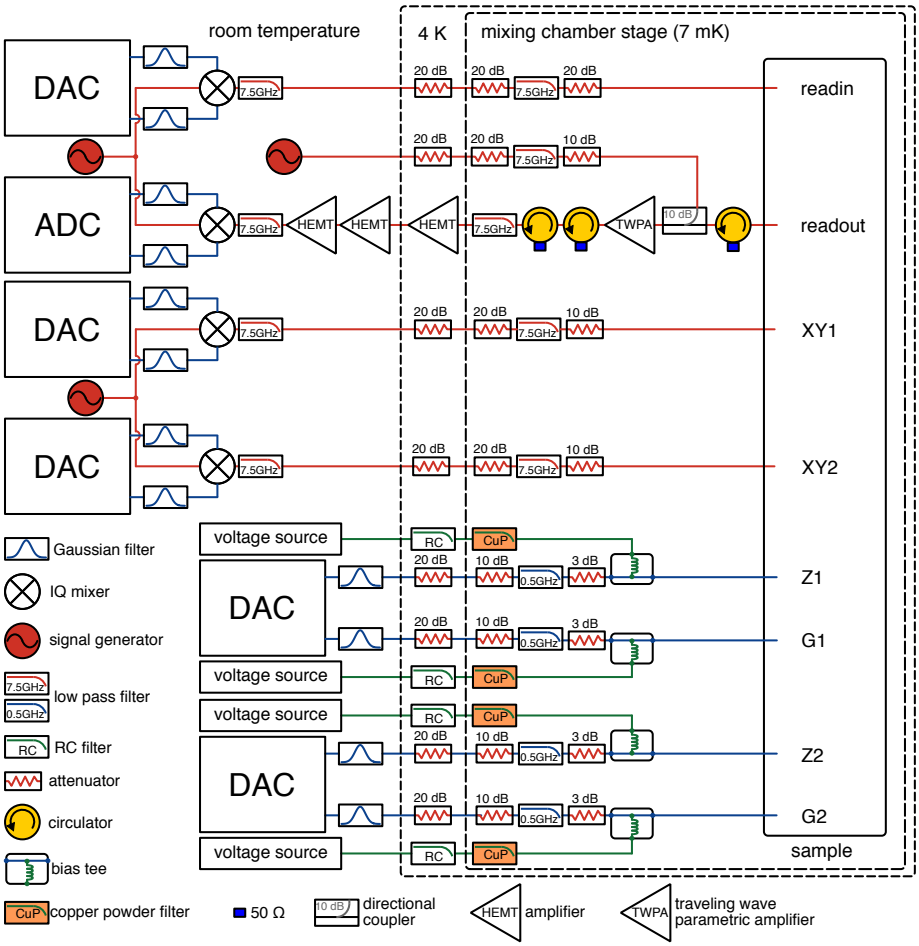

Figure S1: Electronics and wiring. Red lines correspond to radiofrequency (RF) and microwave signals for qubit XY control and measurement, blue lines correspond to intermediate frequency (IF) signals for fast qubit Z or coupler control, and green lines correspond to quasi-DC signals for steady qubit Z or coupler bias offset. The IF and DC signals for each bias channel are combined using a custom-made cryogenic bias tee mounted at the mixing chamber stage.

4 Device Characterization

Each qubit can be tuned from 3 to 7.3 GHz using its Z-control current bias, with full quantum state control using the XY-control microwave drive line, and dispersive readout with a capacitively-coupled readout resonator (*17*).

4.1 Summary of device parameters

In Table S2 we display the characteristics for each qubit Q_1 and Q_2. Parameters preceded by * are design values; others are experimental values.

Parameters	Q_1	Q_2
*Qubit capacitance, C_q	90 fF	90 fF
Qubit junction inductance, L_J	8.34 nH	8.57 nH
*Coupler inductance to ground, L_g	0.2 nH	0.2 nH
*Coupler stray wiring inductance, L_w	0.1 nH	0.1 nH
Coupler junction inductance, L_T	0.57 nH	0.57 nH
Qubit operating frequency, $\omega_q/2\pi$	5.809 GHz	5.731 GHz
Qubit anharmonicity, α	-160 MHz	-162 MHz
Qubit lifetime, T_1	16 μs	11 μs
Qubit Ramsey dephasing time, T_2	0.89 μs	0.85 μs
Readout resonator frequency, $\omega_r/2\pi$	6.4527 GHz	6.3390 GHz
*Readout coupling, $g_r/2\pi$	38 MHz	38 MHz
Readout dispersive shift, κ_r	0.6 MHz	0.8 MHz
$\|g\rangle$ state readout fidelity, F_g	0.984	0.984
$\|e\rangle$ state readout fidelity, F_e	0.950	0.942

* These are design parameters.

Table S2: Device parameters.

4.2 Qubit single-shot readout

We characterize the qubit readout fidelity by turning the coupler for each qubit as close to zero as possible, to isolate the qubit from the rest of the circuit. With the qubit in its equilibrium state (mostly in its ground state $|g\rangle$), we then perform a standard single-shot readout measurement, and record the values of the microwave quadratures I and Q corresponding to the readout result. We accumulate a large number of these events, shown in blue in Fig. S2. We then repeat this process, but precede the measurement with an on-resonant microwave pulse calibrated to put the qubit in its excited state $|e\rangle$. The results of these measurements are shown in orange in Fig. S2. These calibrations allow us to assign any single-shot measurement, based on its de-convolved

I and Q values, to the $|g\rangle$ or $|e\rangle$ state based on which side of the dashed line in Fig. S2 the measurement falls. For Q_1, the $|g\rangle$ state readout fidelity is $F_g = 0.984$, and the $|e\rangle$ state readout fidelity is $F_e = 0.950$. For Q_2, the $|g\rangle$ state readout fidelity is $F_g = 0.984$, and the $|e\rangle$ state readout fidelity is $F_e = 0.942$.

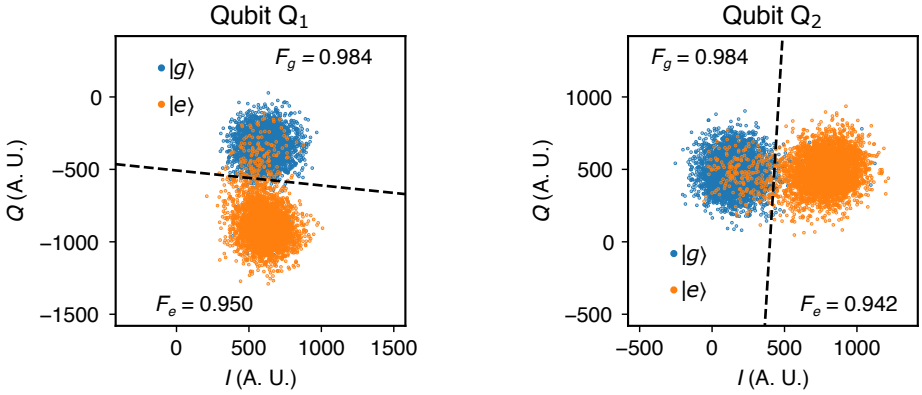

Figure S2: Qubit single-shot readout. A large number of measurements were made with each qubit in either its ground $|g\rangle$ or its excited $|e\rangle$ state, and data accumulated as the blue or orange points respectively. This calibration allows us to assign any given measurement to the ground or excited state, as separated by the dashed lines in the IQ plane. For Q_1, the $|g\rangle$ state readout fidelity is $F_g = 0.984$, and the $|e\rangle$ state readout fidelity is $F_e = 0.950$. For Q_2, the $|g\rangle$ state readout fidelity is $F_g = 0.984$, and the $|e\rangle$ state readout fidelity is $F_e = 0.942$.

4.3 Multimode coupling

The 78 cm-long coplanar waveguide transmission line used in this experiment has a 4 μm-wide center trace and a 2 μm gap to the ground plane on each side, with specific capacitance $\mathscr{C} = 173$ pF/m and specific inductance $\mathscr{L} = 402$ nH/m. Neglecting the coupler, the line is shorted by L_g at its far end, where this inductance is provided by a short segment of transmission line. We absorb this length in the overall transmission line, so that the input impedance is given by

$$Z_{\text{in}} = Z_0 \tanh(\alpha + i\beta)\ell = Z_0 \frac{\tanh\alpha\ell + i\tan\beta\ell}{1 + i\tan(\beta\ell)\tanh(\alpha\ell)}, \tag{S1}$$

where $\alpha + i\beta$ is the complex propagation parameter, and $Z_0 = \sqrt{\mathscr{L}/\mathscr{C}}$ is the characteristic impedance of the transmission line (*31*).

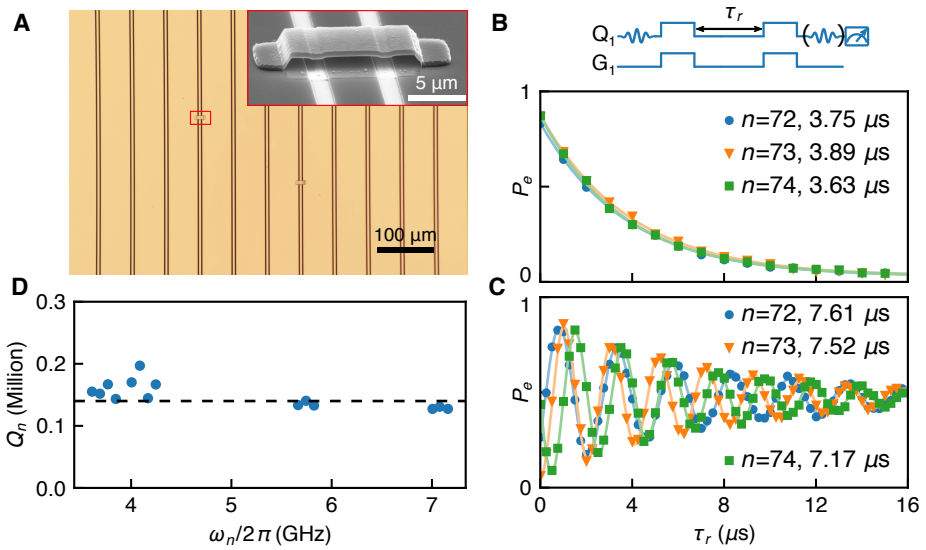

Figure S3: Transmission line characterization. **A** Optical micrograph of a small portion of the transmission line, which has a 4 μm wide center trace and a 2 μm gap to the ground plane on either side. The transmission line meanders are separated by 60 μm, and the line has 390 air-bridge crossovers evenly distributed along the line every 2 mm, suppressing unwanted slot-line modes and other microwave resonances. Inset: Scanning electron micrograph picture of an air-bridge crossover. **B**, **C** The lifetime T_{1n} and Ramsey dephasing time T_{2n} of three of the six resonant modes shown in Fig. 1**D**. We find $T_{2n} \approx 2T_{1n}$, indicating negligible dephasing noise in the transmission line. Solid lines: Fits to each mode's data. Top: Control pulse sequence. **D** Quality factor $Q_n = \omega_n T_{1n}$ measured for different modes from 3.6 GHz to 7.2 GHz. We find that the quality factor is more or less constant over this frequency range, consistent with Eq. (S8), with an average $\langle Q \rangle \sim 1.4 \times 10^5$ as indicated by the horizontal dashed line.

Near the nth mode resonance,

$$\beta\ell = n\pi + \frac{\pi\Delta\omega}{\omega_{\lambda/2}}, \tag{S2}$$

where $\omega_{\lambda/2}$ is the half-wave radial frequency. Near this frequency we have the input impedance

$$Z_{\text{in}} \approx Z_0 \left(\alpha\ell + i\frac{\pi\Delta\omega}{\omega_{\lambda/2}}\right), \tag{S3}$$

where we assume $\alpha\ell \ll 1$, a safe assumption for a superconducting transmission line on a very low-loss substrate such as sapphire.

This impedance is equivalent to a series RLC resonant circuit with equivalent lumped-element parameters

$$\omega_n = n\omega_{\lambda/2}, \tag{S4}$$

$$R_n = Z_0\alpha\ell, \tag{S5}$$

$$L_n = \frac{\pi Z_0}{2\omega_{\lambda/2}} = \frac{1}{2}\mathcal{L}\ell, \tag{S6}$$

$$C_n = \frac{1}{n^2\omega_{\lambda/2}^2 L} = \frac{2\mathcal{C}\ell}{n^2\pi^2}, \tag{S7}$$

$$Q_n = \frac{\omega_n L_n}{R_n} = \frac{\beta}{2\alpha}. \tag{S8}$$

In Fig. S3, we display the transmission line and its characterization. Figure S3**A** shows an optical micrograph of a small portion of the transmission line and a scanning electron micrograph picture of one of the 390 air-bridge crossovers evenly distributed along the line. In Fig. S3**B** and **C**,we use Q_1, weakly coupled to the line, to measure the lifetime T_{1n} and the Ramsey dephasing time T_{2n} of three resonator modes, with $T_{2n} \approx 2T_{1n}$ indicating that dephasing noise is negligible in the channel. In Fig. S3**D**, we show the quality factor $Q_n = \omega_n T_{1n}$ for different modes ranging from 3.6 GHz to 7.2 GHz. We find that Q_n is more or less constant over this span of frequencies, consistent with Eq. (S8), with an average $\langle Q\rangle \sim 1.4 \times 10^5$. Similar quality factors can be achieved with superconducting coaxial cables (*32*), so in principle the transmission line here can be replaced by a superconducting cable for inter-chip quantum communication. Note that for planar transmission lines that include crossovers where an SiO_2 dielectric is left as a support structure, measurements find quality factors roughly one order of magnitude smaller than here (*27*). Removing the SiO_2 crossover scaffold, as was done here, is therefore an important step for reducing transmission line loss.

The effective mutual inductance between the qubit and the transmission line is given by (*15*)

$$M = \frac{L_g^2}{2L_g + L_w + L_T/\cos\delta}. \tag{S9}$$

Note we have added the L_w term as compared to ref. (*15*), which in our circuit has a value $L_w \approx 0.1$ nH and cannot be ignored when L_T becomes very small. In the harmonic limit and assuming weak coupling, the coupling between the qubit Q_i and the nth mode is

$$g_{i,n} = -\frac{M}{2}\sqrt{\frac{\omega_q\omega_n}{(L_g + L_J)(L_g + L_n)}}. \tag{S10}$$

We can see that through its dependence on ω_n, $g_{i,n} \propto \sqrt{n}$, a well-known result for multimode coupling. In the experiments here, only the modes with $\omega_n \sim \omega_q$ are relevant, where $n \sim 70$. As the range of n ($\sim \pm 5$) is small, the variation of g_i with n is only a few percent, so the dependence of g_i on n can be ignored.

The analytical result Eq. (S10) agrees well with the experimental data, using $L_T = 0.57$ nH. The comparison between this calculation and the measured coupling for both qubits is shown in Fig. S4. Maximum coupling occurs at junction phase $\delta = \pi$, where we find $|g_{i,\max}|/2\pi \approx 45$ MHz for qubit frequencies near 5.8 GHz. The coupling can be turned off by setting $\delta = \pi/2$, making $L_T/\cos\delta$ very large. We turn the couplers off when characterizing the qubits.

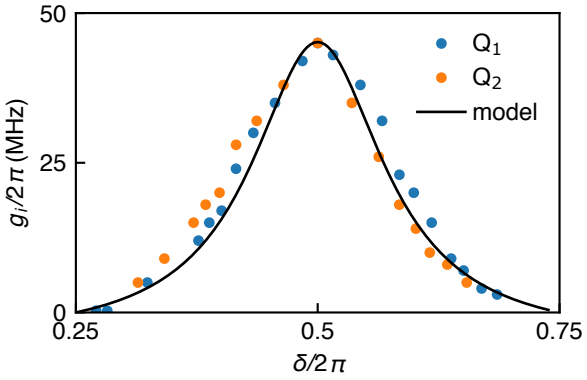

Figure S4: Coupling strength versus coupler junction phase δ. We measure the qubit spectrum at different coupler bias values, similar to Fig. 3**A**, and fit the spectrum to obtain the coupling strength g_i. The maximum coupling is about 45 MHz for both qubits.

4.4 Coupler-generated qubit frequency shift

The tunable couplers used here ideally only change the qubit-transmission line coupling strength. However, changes in the coupler junction inductance L_T affect the qubit resonance frequency, as can be seen from the circuit diagram in Fig. 1B. This is accounted for by including the coupler mutual inductance M, Eq. (S9), in the calculation of the qubit frequency, through its effect on the qubit inductance L_q, which is given by

$$L_q = L_J + L_g - M. \tag{S11}$$

In the experiment, $\omega_n \sim \omega_q \approx \dfrac{1}{\sqrt{(L_g + L_J)C_q}}$, so we can use Eq. (S10) to relate the mutual inductance to the coupling,

$$M = -2g_i\sqrt{C_q(L_g + L_n)}(L_g + L_J). \tag{S12}$$

The qubit inductance is then given by

$$L_q = (L_g + L_J)\left(1 + 2g_i\sqrt{C_q(L_g + L_n)}\right), \tag{S13}$$

so that the qubit frequency including the coupler is given by

$$\begin{aligned}
\omega_q' &= \frac{1}{\sqrt{L_q C_q}} && \text{(S14)}\\
&= \frac{1}{\sqrt{(L_g + L_J)C_q}}\frac{1}{\sqrt{1 + 2g_i\sqrt{C_q(L_g + L_n)}}} && \text{(S15)}\\
&\approx \omega_q\left(1 - g_i\sqrt{C_q(L_g + L_n)}\right). && \text{(S16)}
\end{aligned}$$

We therefore find that the qubit frequency is shifted by the coupler by an amount

$$\Delta\omega_q = -g_i\omega_q\sqrt{C_q(L_g + L_n)} = -g_i\sqrt{\frac{L_g + L_n}{L_g + L_J}}. \tag{S17}$$

Similarly, we can show that the transmission line's nth mode resonant frequency is shifted by

$$\Delta\omega_n = -g_i\omega_n\sqrt{C_n(L_g + L_J)} = -g_i\sqrt{\frac{L_g + L_J}{L_g + L_n}}. \tag{S18}$$

Because $L_n \gg L_J$, $\Delta\omega_q$ is much larger than $\Delta\omega_n$. According to Fig. S4, with maximum coupling $g_{i,\max}/2\pi = 45$ MHz, the qubit frequency can be shifted by as much as -200 MHz by tuning the coupling from off to its maximum value. This frequency shift can be compensated by adjusting the qubit junction inductance L_J accordingly, as was done in the measurements.

In the experiments shown in Fig. 3**A** and **B**, we bias G_1 to set its coupling to its maximum value, which changes the qubit frequency through Eq. (S17). At the same time, we adjust Q_1's Z bias, which changes the qubit junction inductance L_J. The net qubit frequency is determined by the combination of these two effects, and is calibrated by fitting the response in Fig. 3**A**. The data in Fig. 3**C** represent a special case of the data in Fig. 3**B**, where the qubit Z bias is set to zero, keeping L_J fixed, as represented by the horizontal line after the π pulse in Q_1's control sequence. However, the qubit frequency is still affected by the coupler. This impacts the itinerant photon capture efficiency, and must be accounted for in the simulations (see the Numerical Simulations section below).

In Fig. 3**D**, to optimize the itinerant photon capture, we adjust the qubit's Z bias to change L_J while tuning the coupling, such that the change of L_J and M cancel each other out, and the qubit frequency is fixed (ideally) during the photon emission and capture process. The two convolution pulses after the π pulse in Q_1's control sequence represent this counteracting Z bias. In Fig. 4**A**, we similarly apply Z bias pulses to both qubits while tuning the couplers, as shown by the control pulse sequences in the inset. These bias pulses not only counteract the frequency shift from the coupler, but also adjust the qubit frequencies to match each other, as the operating frequencies are not the same for the two qubits.

5 CHSH Bell inequality

After generating a Bell state using either the relay mode method or the shaped itinerant photon method, we perform the CHSH form of Bell inequality test. This is done by measuring Q_1 along

either direction a, which is chosen to be the x axis on the Bloch sphere (see inset to Fig. 3**D**), or along direction a', which is chosen to be the Bloch sphere y axis. At the same time, we measure Q_2 along direction b or b', where b is on the Bloch sphere equator, rotated by an angle θ about the z axis with respect to a, and b' is perpendicular to b. For each choice of axes (q_1, q_2) (where q_1 can be a or a', q_2 can be b or b'), we accumulate many measurements of the two qubits, and calculate the quantum correlation $E(q_1, q_2) = P_{gg} + P_{ee} - P_{ge} - P_{eg}$, where the subscript ge for example means those measurement outcomes where Q_1 was measured to be in $|g\rangle$ along q_1 and Q_2 was measured to be in $|e\rangle$ along q_2. Given the set of four quantum correlators for a given angle θ, we then define the CHSH correlation $S(\theta) = E(a, b) - E(a, b') + E(a', b) + E(a', b')$. The CHSH inequality states that $|S| \leq 2$ for a classical system, while quantum physics predicts $|S| \leq 2\sqrt{2}$. For an ideal Bell state, S is maximized when $a \perp a'$, $b \perp b'$, and a is at $\angle 45^\circ$ with respect to b. In the experiments here however, S is maximized at a different value of θ, due to dynamic phase accumulation in the qubits during state preparation.

6 Numerical Simulations

6.1 Multimode model simulation

We performed extensive numerical simulations to better understand and calibrate the experiment. These simulations used the following rotating-frame qubit-multimode Hamiltonian:

$$H/\hbar = \sum_{i=1,2} \Delta\omega_i \sigma_i^\dagger \sigma_i + \sum_{n=1}^{N} \left(n - \frac{N+1}{2} \right) \omega_{\mathrm{FSR}} a_n^\dagger a_n + \sum_{i=1,2} \sum_{n=1}^{N} g_i \left(\sigma_i a_n^\dagger + \sigma_i^\dagger a_n \right), \quad \text{(S19)}$$

where σ_i and a_n are the annihilation operators for qubit Q_i and photons in the nth standing wave mode, respectively, $\Delta\omega_i$ is the qubit frequency detuning in the rotating frame, and N is the number of standing modes included in the simulation.

In Fig. 2, where the coupling g_i is weak, we included five standing modes in the simulations, and assumed the coupling is turned on and off abruptly. Decoherence is taken into account

using the Lindblad master equation. According to ref. (*33*), the effective dephasing time is enhanced by $\sqrt{2}$ when transferring the quantum state from one qubit to the other, because the dephasing noise at each qubit is uncorrelated. Taking this into account, we find that the simulation agrees well with the experiment. According to the simulations, more than half of the infidelity is attributed to dephasing noise. Simulations that take $T_2 = 10\ \mu$s for both qubits give a state transfer process fidelity of $\mathcal{F}_1^p = 0.977$, a Bell state fidelity $\mathcal{F}_1^s = 0.983$ and a concurrence $\mathcal{C} = 0.980$. The remaining 2 percent infidelity is attributed to energy dissipation and interference from adjacent modes.

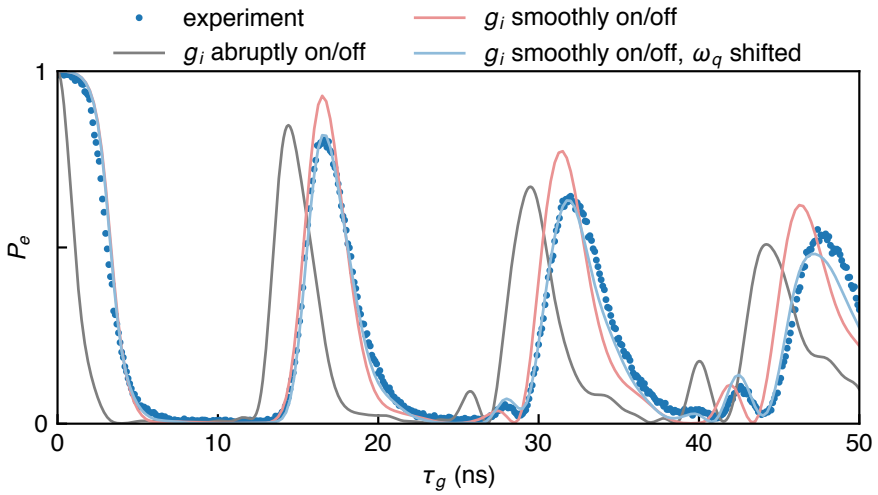

Figure S5: Different simulations for the experiment shown in Fig. 3**C**. Simulation details are given in the text.

For the simulations in Fig. 3 and Fig. 4, we include ten standing modes, and the coupling is strong enough that the finite rise and fall time of the control signal has to be taken into account. In the simulations, we assume the phase due to the external flux threaded through the coupler loop δ_{ext} is proportional to the control pulse amplitude. The coupler junction phase δ is related to δ_{ext} by (*34*)

$$\delta_{\text{ext}} = \delta + \frac{2L_g + L_w}{L_T} \sin\delta. \tag{S20}$$

The coupler is first biased with a DC current to give

$$\delta_{\text{ext}} = \delta_{\text{off}} = \pi/2 + \frac{2L_g + L_w}{L_T}, \tag{S21}$$

where $\delta = \pi/2$ and $g_i = 0$. We then use the high-speed control signal output of the DAC to rapidly tune the coupling g_i, combined with a separate DC current source via a bias tee mounted on the mixing chamber stage. The filter in the DAC output has a Gaussian spectrum, so that when we generate a rectangular output signal to set the coupling to its maximum value (where $\delta_{\text{ext}} = \delta = \pi$), the actual output is a convolution of the filter Gaussian and the rectangular control signal. The external flux then changes as

$$\delta_{\text{ext}}(t) = (\pi - \delta_{\text{off}}) \left(G(w_{\text{FWHM}}, t) \circledast \text{Rect}(\tau, t)\right)(t) + \delta_{\text{off}}, \tag{S22}$$

where $G(w_{\text{FWHM}}, t)$ is a Gaussian function with a full-width at half-maximum (FWHM) of w_{FWHM}, and $\text{Rect}(\tau, t)$ is a rectangle function with unit amplitude from 0 to τ. We then solve Eq. (S20) to obtain $\delta(t)$, and use this result in Eq. (S10) to obtain $g_i(t)$.

In Fig. S5, we compare the experimental data with different assumptions for the simulations. The light black line treats the coupling as switched abruptly between its on and off values, i.e. we assume $w_{\text{FWHM}} = 0$. Here we see that the experimental data lags 2 ns behind the simulation. The light red line corresponds to setting $w_{\text{FWHM}} = 2$ ns, which is determined by the bandwidth of the control signal output filter, and agrees well with the experimental data, except the photon recapture probability is too high. This is because the qubit frequency is shifted by as much as -200 MHz when tuning the coupling to the maximum, see Eq. (S17), not accounted for in this simulation. The light blue line takes this frequency shift into account and is in good agreement with the experiment.

In Fig. 3**D**, in addition to the Gaussian filter, we program the control signal output to adjust w_{FWHM} to 3 ns to optimize the photon catch probability, and compensate the qubit frequency

shift with the qubit Z control bias. This frequency compensation is assumed to be perfect in the simulation.

In Fig. 4**A**, although the couplings for both qubits are turned on simultaneously, it takes $T_\ell = 6.3$ ns for the itinerant photon to reach Q_2. Therefore, from the viewpoint of the itinerant photon, the Q_2 coupling is turned on T_ℓ later than that of Q_1. This time lag is taken into account by setting $g_2(t) = g_1(t - T_\ell)$ in the simulation.

6.2 Input-output theory simulation

The multimode simulations agree well with the data, because the ratio of the maximum coupling and the free spectral range $g_{i,\max}/\omega_{\rm FSR}$ is less than or of order one, so that the number of modes N needed for the simulation (and thus the Hilbert space dimension) is not too large. However, as the transmission line length ℓ increases, $g_{i,\max}/\omega_{\rm FSR}$ increases as $\sqrt{\ell}$, so that to maintain numerical accuracy, N has to increase, and the Hilbert space dimension increases exponentially; for large ℓ this method quickly becomes impractical. An alternative is to use input-output theory (*23, 24*), which treats the mode spectrum in the transmission line as continuous, and thus is well-suited for simulating the dynamics with large $g_{i,\max}/\omega_{\rm FSR}$, as long as reflections can be ignored (we note that extensions of input-output theory allow some reflections to be included, see e.g. ref. (*35*)). Here we apply the quantum Langevin equations to the state transfer process in Fig. 4**A**:

$$\frac{\mathrm{d}\sigma_1}{\mathrm{dt}} = -i\Delta\omega_1\sigma_1 - \frac{\kappa_1(t)}{2}\sigma_1, \tag{S23}$$

$$\frac{\mathrm{d}\sigma_2}{\mathrm{dt}} = -i\Delta\omega_2\sigma_2 - \frac{\kappa_2(t)}{2}\sigma_2 + \sqrt{\kappa_2(t)\kappa_1(t-T_\ell)}\sigma_1(t-T_\ell), \tag{S24}$$

where κ_i is the decay rate of each qubit to the transmission line. Note we have replaced the annihilation field operator in refs. (*23, 24*) by the qubit annihilation operator; this replacement is valid because there is at most one excitation in the system during the simulation. The value

of κ_i can be obtained by treating the transmission line as a lumped element resistance Z_0 to ground, then transforming the linear circuit to an equivalent series RLC resonant circuit with a series resistance R_s, see Fig. S6. The quality factor of this series RLC resonant circuit is (*31*)

$$Q = \frac{\omega_q(L_J + L_s)}{R_s}, \tag{S25}$$

so the decay rate κ_i is then given by

$$\kappa_i = \frac{\omega_q}{Q} = \frac{R_s}{L_J + L_s}. \tag{S26}$$

Note that treating the transmission line as a lumped element resistance is valid only when the dynamics are completed within the round-trip time $2T_\ell$, so that there are no retro-reflections.

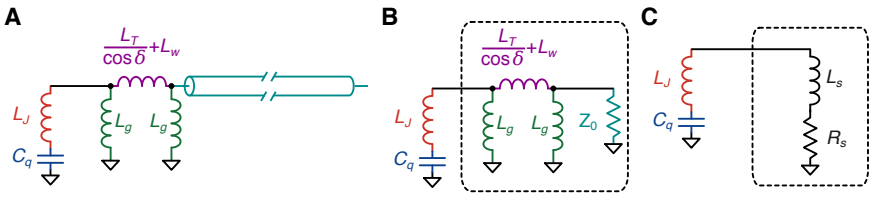

Figure S6: Linear circuit transformation for calculating the qubit decay rate into the transmission line. **A** Linear circuit model for a qubit connected to the transmission line by a tunable coupler. **B** Assuming no reflection, we can treat the transmission line as a lumped element resistance Z_0. **C** Transforming the circuit in **B** to an equivalent series RLC circuit with series resistance R_s. The circuit segments in the dashed rectangles in **B** and **C** have equal impedances at angular frequency ω_q. From this we can calculate the qubit decay rate κ_i into the transmission line.

We obtain the time evolution of δ as in the multimode model simulation, from which we calculate $\kappa_i(t)$, then insert this result into the quantum Langevin equations Eqs. (S23) and (S24) to solve for the dynamics; see Fig. S7. The qubit frequency shift is assumed to be perfectly compensated in the simulation, so we take $\Delta\omega_i = 0$. The simulation agrees well with the data within the round-trip time $2T_\ell$, then starts to deviate because of reflections. Note the state transfer process fidelity is not affected by changes in the transmission line length ℓ in this simulation, unless the channel decoherence is taken into account.

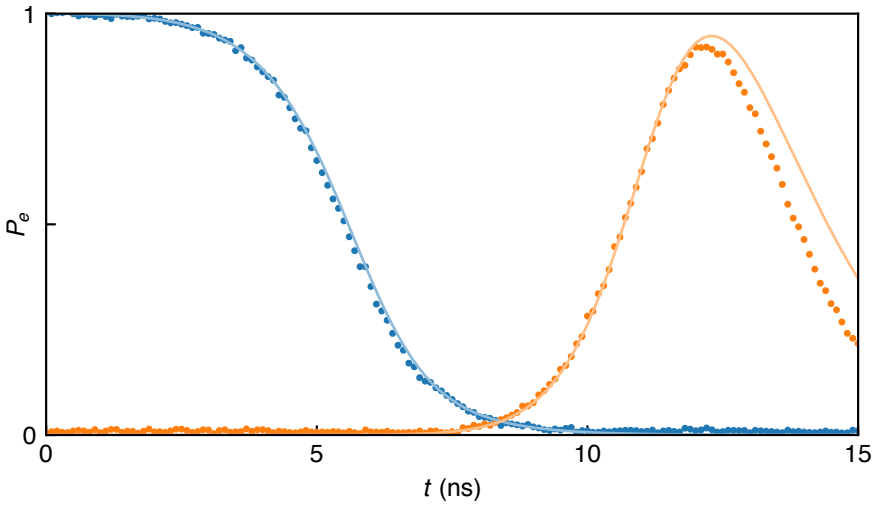

Figure S7: Input-output theory simulation for the state transfer process in Fig. 4**A** in the main text. The simulations (solid lines) fits well with the data within the round-trip time $2T_\ell$, then starts to deviate after $2T_\ell$ because of the retro-reflection.

In the experiments in refs. (*7*–*9*), a circulator was interposed in the transmission line connecting the two communication nodes, eliminating reflections and at the same time providing a means to probe the emitted photon waveform, allowing tune-up of the emission profile to achieve the desired symmetric envelope. In our itinerant photon experiment, we have no direct means to probe the emitted photon envelope. However, according to input-output theory, $|\langle\sqrt{\kappa_1}\sigma_1\rangle|^2$ is the squared mean field amplitude of the itinerant photon emitted from Q_1. In Fig. S8 we show this quantity, calculated from the simulation results shown in Fig. S7, these results being themselves close to the experimental data. We see that the emitted photon envelope is relatively symmetric, even with the simple coupler control pulse used in the experiment. This symmetry is the key reason that we are able to achieve such high-fidelity state transfers using the itinerant photon method.

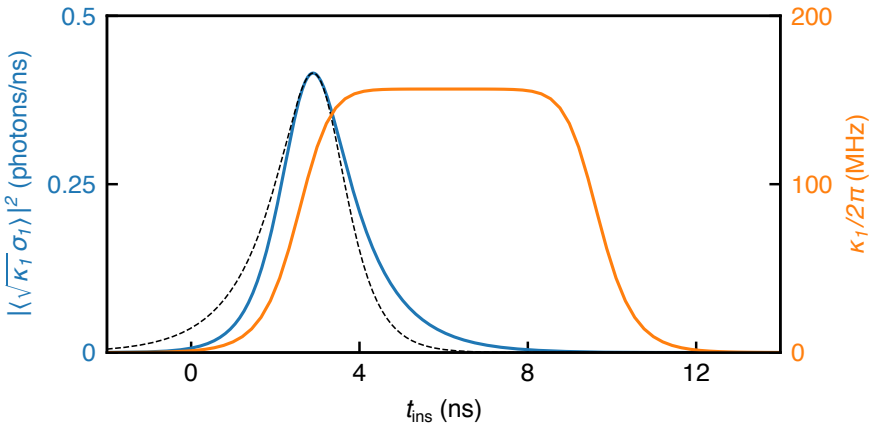

Figure S8: Emitted photon envelope estimated from simulations. The horizontal axis is the instantaneous time $t_{\rm ins}$ of the dynamic evolution, calculated for a control pulse width set to $t = 12.2$ ns for optimized state transfer. Left axis (blue) shows the emitted photon envelope $|\langle\sqrt{\kappa_1}\sigma_1\rangle|^2$; right axis (orange) shows the qubit decay rate $\kappa_1/2\pi$. Black dashed line is the time-reversed form for the emitted photon envelope, reasonably close to the blue forward-time envelope.

7 Optimized itinerant photon catch for Q_2

In Fig. 3**D** we show the data for optimizing qubit Q_1's itinerant photon "catch" process. Here we show the analogous data for qubit Q_2, see Fig. S9. The maximum photon catch probability is found to be 0.917 ± 0.006.

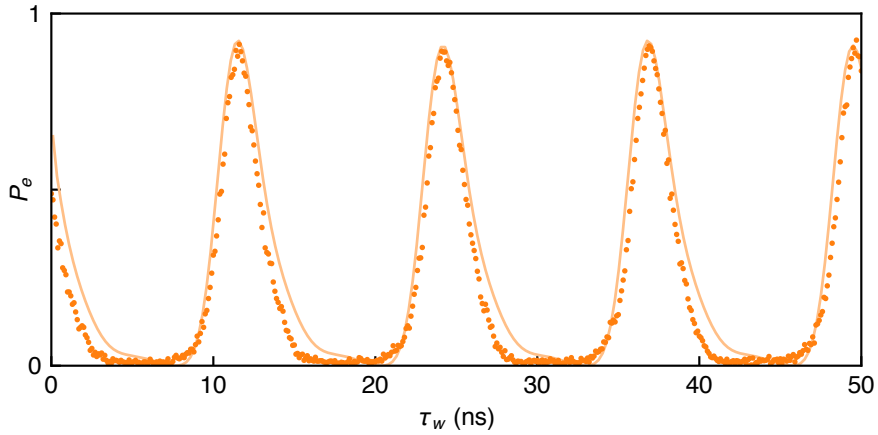

Figure S9: Optimized itinerant photon catch process for qubit Q_2, analogous to Fig. 3D in the main text with a slight adjustment to the control pulse optimization. The capture probability is found to be 0.917 ± 0.006. Solid line is simulation.